

# Enhanced Nanoparticle Size Control by Extending LaMer's Mechanism

Erika C. Vreeland,<sup>†</sup> John Watt,<sup>†</sup> Gretchen B. Schober,<sup>†</sup> Bradley G. Hance,<sup>†</sup> Mariah J. Austin,<sup>†</sup> Andrew D. Price,<sup>‡</sup> Benjamin D. Fellows,<sup>†</sup> Todd C. Monson,<sup>†</sup> Nicholas S. Hudak,<sup>†</sup> Lorena Maldonado-Camargo,<sup>§</sup> Ana C. Bohorquez,<sup>‡</sup> Carlos Rinaldi,<sup>§,‡</sup> and Dale L. Huber<sup>\*,†</sup>

<sup>†</sup>Sandia National Laboratories, Albuquerque, New Mexico 87185, United States

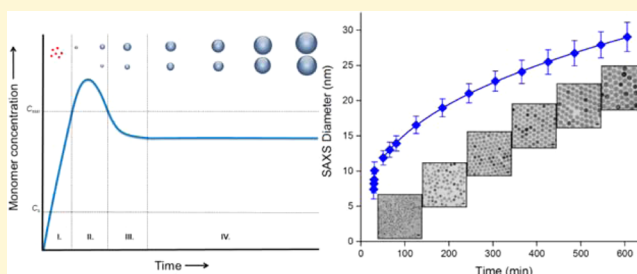
<sup>‡</sup>Senior Scientific LLC, Albuquerque, New Mexico 87106, United States

<sup>§</sup>Department of Chemical Engineering, University of Florida, Gainesville, Florida 32611, United States

<sup>‡</sup>J. Crayton Pruitt Family Department of Biomedical Engineering, University of Florida, Gainesville, Florida 32611, United States

## Supporting Information

**ABSTRACT:** The synthesis of well-defined nanoparticle materials has been an area of intense investigation, but size control in nanoparticle syntheses is largely empirical. Here, we introduce a general method for fine size control in the synthesis of nanoparticles by establishing steady state growth conditions through the continuous, controlled addition of precursor, leading to a uniform rate of particle growth. This approach, which we term the “extended LaMer mechanism” allows for reproducibility in particle size from batch to batch as well as the ability to predict nanoparticle size by monitoring the early stages of growth. We have demonstrated this method by applying it to a challenging synthetic system: magnetite nanoparticles. To facilitate this reaction, we have developed a reproducible method for synthesizing an iron oleate precursor that can be used without purification. We then show how such fine size control affects the performance of magnetite nanoparticles in magnetic hyperthermia.



## INTRODUCTION

Magnetic nanoparticles are one of the most promising classes of particles for biomedical applications, and among these magnetite ( $\text{Fe}_3\text{O}_4$ ) nanoparticles are an exciting candidate, due to their low toxicity and strong magnetic properties.<sup>1–4</sup> For the effective application of magnetic nanoparticles, fine and reproducible size control is essential.<sup>5,6</sup> For example, a number of biomedical applications (e.g., magnetic relaxometry,<sup>7,8</sup> magnetic particle imaging (MPI),<sup>9,10</sup> magnetic hyperthermia<sup>11,12</sup>) rely on the superparamagnetic relaxation of magnetic nanoparticles. Superparamagnetic relaxation is a thermally-activated process where the relaxation time ( $\tau$ ) follows Arrhenius kinetics ( $\tau = \tau_0 e^{(-K_1 V/kT)}$ ). The activation energy is the product of the magnetocrystalline anisotropy ( $K_1$ ) and particles volume ( $V$ ), which means the relaxation varies with size as  $e^{V^3}$ , an extraordinarily strong size dependence. Therefore, even small variations in the size and size distribution of magnetic nanoparticles can render them ineffective in biomedical applications.

Currently, there is one dominant method for the synthesis of magnetite nanoparticles: the thermal decomposition of iron oleate in high boiling point solvents.<sup>13–17</sup> This method is capable of producing large quantities of highly magnetic nanoparticles with low size and shape dispersity. However,

there remains a series of challenges to the systematic control and reproducibility in their synthesis. First, the favored precursor, iron oleate, exists as a nonstoichiometric mixture, which resists purification, and batch-to-batch variations in the precursor can lead to significant variations in product size and size distribution.<sup>18</sup> Second, systematic control of size requires control over the number of nuclei formed in the nucleation event, which is extremely challenging due to the complexity of the kinetics of nucleation.<sup>17,19</sup> Finally, subtle variations in nucleation, occurring in reactions intended to be identical, lead to significant differences in final products in ways that are difficult to observe or predict.

Here, we propose a new approach to the synthesis of magnetite nanoparticles, which we term the “extended LaMer mechanism”. This approach involves the constant addition of precursor to the reaction solution resulting in uniform, continuous growth to arbitrarily large sizes. Control of particle size is achieved simply by varying the reaction duration and hence volume of added precursor and yields highly crystalline nanoparticles with subnanometer precision and very low size dispersity. This method allows for a high level of reproducibility.

Received: June 30, 2015

Revised: August 14, 2015

Published: August 17, 2015

bility, which we demonstrate with several reactions using separate batches of precursor. We then demonstrate how a uniform rate of growth allows the size of the nanoparticle product to be easily predicted. Finally, we systematically vary nanoparticle size and demonstrate the significant impact this has on the performance of the nanoparticles in magnetic hyperthermia, a representative biomedical application. While some aspects of this work are necessarily specific to the system at hand, the general synthetic approach is applicable to a wide range of other nanoparticle species.

## RESULTS AND DISCUSSION

**Extended LaMer Mechanism.** Nanoparticle synthesis is often described using the classical LaMer mechanism, which we compare to the proposed extended LaMer mechanism for nanoparticle synthesis (Figure 1). In his seminal study, LaMer described a reaction system using a plot of a notional monomer concentration versus time (Figure 1a).<sup>20</sup> Here, monomer refers to a reacted species that is dissolved in solution but is unstable and able to form or attach to a particle without a significant energy barrier. A reaction following the LaMer mechanism can be divided into three stages where (I) the monomer is produced and accumulates in solution, which becomes supersaturated, but no particles are present; (II) the monomer concentration exceeds the critical level of supersaturation where nucleation is energetically favorable ( $C_{\min}$ ), and particles nucleate. The burst of nucleation partially relieves the supersaturation, and the concentration of monomer passes back below  $C_{\min}$ , and the reaction enters stage III, where growth of nanoparticles continues without further nucleation. Though not part of LaMer's original mechanism, growth after the exhaustion of precursor can also occur through the process of Ostwald ripening, where larger particles grow at the expense of smaller particles, thereby lowering the overall surface energy of the system.<sup>21–23</sup> It is generally accepted that additional nucleation events and Ostwald ripening in stage III lead to large size dispersity in the final nanoparticle product and should therefore be avoided. The LaMer mechanism occurs in a closed system, and the number of nanoparticles grown is defined in the nucleation event. The maximum particle size that can be achieved through this mechanism is then set by the amount of material originally introduced divided by the number of nuclei formed in stage II. While the number of nuclei formed can undoubtedly be altered through the choice of reaction conditions, systematic, predictable control of nucleation is extremely difficult.

Our proposed extended LaMer mechanism (Figure 1b) is an open system involving continuous addition of precursor, which matches the classic LaMer mechanism in stages I and II but diverges following the nucleation event. Here, we introduce a distinct stage III and include a stage IV. In stage III of the extended LaMer mechanism, the concentration of monomer decreases, much like in the classic LaMer mechanism, as the high concentration of monomer is consumed and growth of the nanoparticles occurs. However, because of the continuous addition of precursor, the production of monomer can be maintained indefinitely. At some point, the consumption of monomer by the growing nanoparticles becomes equal to the rate of production of monomer, and the monomer concentration reaches a steady state. This begins stage IV, the steady-state growth of nanoparticles. The advantage of this approach is that this fourth stage can be extended for an arbitrarily long time, allowing the growth of a wide range of particle sizes while

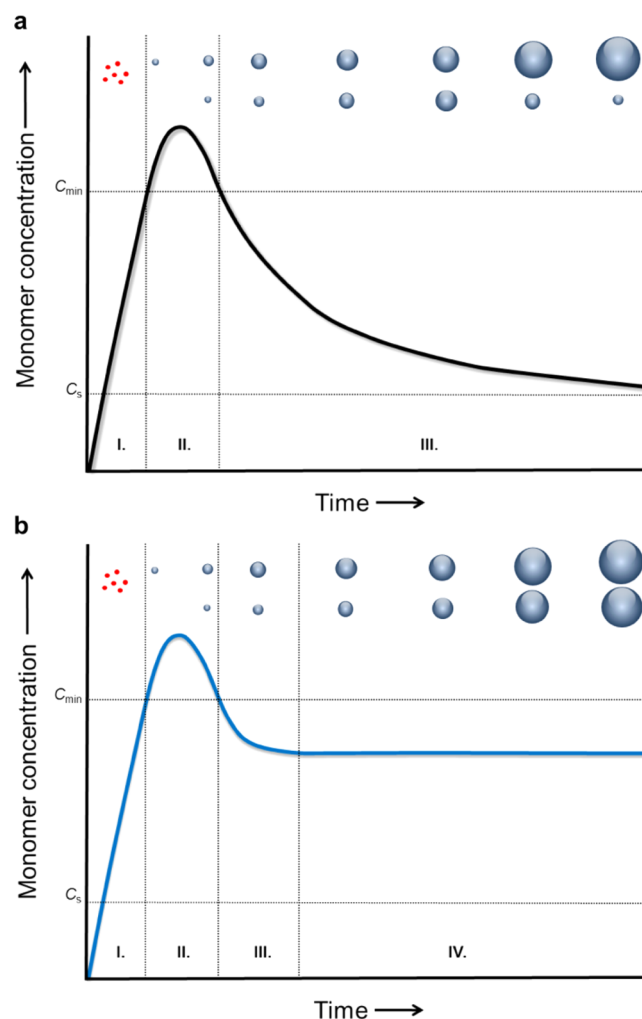


**Figure 1.** (a) Classic LaMer mechanism for nanoparticle growth can be explained in three stages: stage I, the monomer concentration increases to the critical supersaturation concentration ( $C_{\min}$ ) required for nucleation. Stage II, the monomer saturation is partially relieved by the nucleation event. Stage III, the monomer concentration drops below the level required for nucleation, and particle growth proceeds by addition of the monomer to the particle surface. With a limited supply of monomer available, the monomer concentration approaches the lower solubility limit ( $C_s$ ), and additional growth proceeds by Ostwald ripening. (b) The proposed Extended LaMer mechanism for nanoparticle growth with enhanced size control. Stages I and II mimic the classic LaMer mechanism. However, because of the constant addition of precursor, stage III does not approach the solubility limit but drops only to a steady-state concentration. This introduced a new stage of growth, stage IV, where a steady state monomer concentration yields continuous growth of nanoparticles to arbitrarily large sizes with tight size dispersity.

maintaining low size dispersity. Additionally, since the growth rate is constant in this stage, the reaction is not only reproducible, but also predictable. Real time, or near real time monitoring of particle size allows one to calculate a growth rate and then extrapolate to determine when to stop a reaction to achieve a desired particle size. Ostwald ripening is avoided by having a steady concentration of monomer species due to the continuous and controlled precursor addition. Furthermore, by maintaining the level of supersaturation below  $C_{\min}$ , no further nucleation events occur. This yields continuous and uniform growth of nanoparticles, resulting in very low size and shape

dispersity, even at large nanoparticle sizes. This leads to a dramatic change in the method of size control, where size can now be systematically varied by merely changing the reaction time.

To apply the extended LaMer approach to the synthesis of magnetite nanoparticles, a reproducible and stoichiometric precursor was first needed. To achieve this, the formation of iron oleate was investigated in situ by Fourier transform infrared (FTIR) experiments (for full analysis, see [Supporting Information](#), Figures S1–S3). Here, we observed a “plateau of stability” in its formation, corresponding to complete conversion of starting materials to the iron oleate intermediate, but preceding particle nucleation. By quenching its formation on this plateau, the iron oleate intermediate could be used directly as the precursor for nanoparticle synthesis without any further purification or manipulations steps. Since we know the amount of iron added and the entire intermediate is introduced in the subsequent reaction, we have a stoichiometric precursor regardless of the binding environment of the oleate ligand on the iron center.<sup>18</sup> To form magnetite nanoparticles, the iron oleate intermediate (0.22 M diluted in octadecene) was slowly dripped (3 mL/h) into a round-bottom flask containing a high boiling point solvent (docosane, 2.5 mL) and excess oleic acid (2.5 mL).

To monitor the reaction progression, small aliquots (100  $\mu$ L) were withdrawn from the reacting mixture. The removal of an aliquot quenched nanoparticle growth due to a rapid drop in temperature, which provided a snapshot of the nanoparticles in the continuing reaction.

**Size Controlled Nanoparticle Synthesis Using the Extended LaMer Mechanism.** A selection of the nanoparticle aliquots was then analyzed by transmission electron microscopy (TEM) ([Figure 2](#)). The nanoparticles are spherical in shape and are single crystal ([Figure S4](#)) and maintain this structure throughout the course of the reaction. Histograms from the size analysis of 1000 nanoparticles (per aliquot) are shown in [Figure 2](#), panel i, along with their standard deviation ( $\sigma$ ) and coefficient of variation ( $\sigma/\mu$ ). Full structural analysis is given in [Supporting Information](#), Figures S5–S7. Briefly, X-ray diffraction (XRD) measurements indicated the formation of highly crystalline magnetite ([Figure S5](#)). The magnetite structure was further confirmed by measuring the temperature-dependent magnetization of the particles using superconducting quantum interference device (SQUID) magnetometry ([Figures S6 and S7](#)). These experiments showed that 22.7 nm nanoparticles, for example, had a saturation magnetization,  $M_{\text{sat}}$  of 70  $\text{Am}^2/\text{kg}$   $\text{Fe}_3\text{O}_4$ , a value that is more than 75% of the bulk value.<sup>24</sup>

For quantitative discussions of particle growth, sizes were determined by small-angle X-ray scattering (SAXS) ([Figure 3](#)). SAXS could be performed in less than 15 min per aliquot, without purification, which allowed for near real time measurement. [Figure 3](#), panel a shows a typical model fit of the raw SAXS data plotted against  $Q$ , where  $Q = 4\pi \sin(\theta)/\lambda$ , along with residuals. The data were modeled using a spherical form factor and assuming a Gaussian size distribution, as observed in TEM. [Figure 3](#), panel b shows the fitted scattering curve for each aliquot taken over the course of the reaction. Each scattering curve possesses a smooth trace at low  $Q$  with no observed correlation peak, which indicates well stabilized and isolated nanoparticles.<sup>25</sup> As the reaction progresses, a minimum appears and shifts to lower  $Q$ , indicating particle growth. The emergence of several additional minima in the

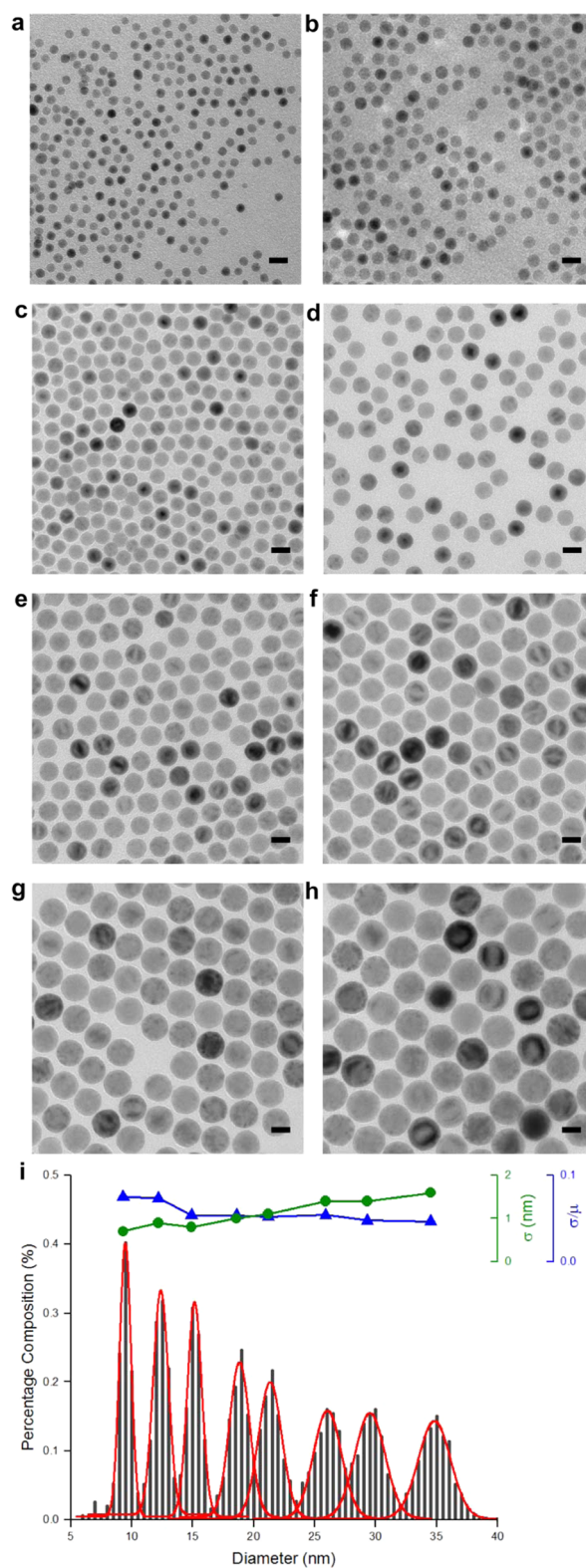


**Figure 2.** TEM images of magnetite nanoparticles synthesized using the extended LaMer approach. Nanoparticle sizes are  $9.3 \pm 0.7$  nm,  $12.2 \pm 0.9$  nm,  $14.9 \pm 0.8$  nm,  $18.6 \pm 1.0$  nm,  $21.2 \pm 1.1$  nm,  $25.9 \pm 1.4$  nm,  $29.3 \pm 1.4$  nm, and  $34.5 \pm 1.6$  nm for images a–h, respectively. All scale bars are equal to 20 nm. (i) Histograms made from analysis of nanoparticle size by TEM, along with standard deviation ( $\sigma$ ) and coefficient of variation ( $\sigma/\mu$ ).



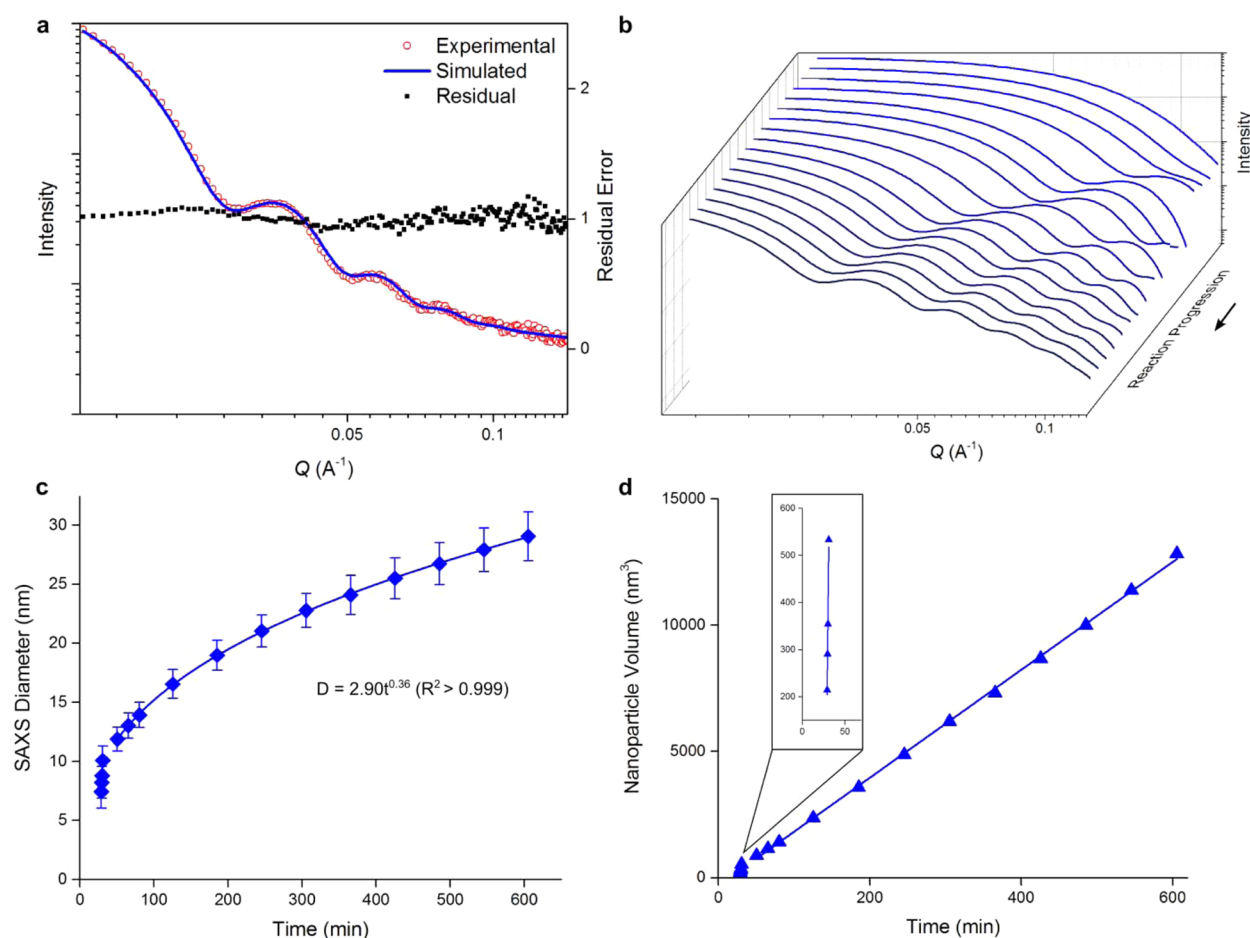


**Figure 3.** SAXS measurements for the formation of magnetite nanoparticles using the extended LaMer approach. (a) A typical SAXS measurement of an aliquot of magnetite nanoparticles showing the experimental raw data, the simulated fit, and the simulation residuals. (b) Plot of simulated intensities of each aliquot taken during the course of the reaction showing an increase in nanoparticle size with tight size dispersity. (c) Plot of calculated SAXS diameter against reaction time. (d) Plot of nanoparticle volume against reaction time with a close-up of the first four aliquots measured shown in the inset.

scattering trace of later aliquots indicates that the nanoparticles match closely with the chosen spherical form factor and possess an incredibly tight size distribution.

The calculated SAXS diameter ( $D$ ) of all aliquots is plotted against reaction time in Figure 3c, panel c. Immediately after nucleation, we observe a rapid increase in nanoparticle size up to 10 nm, after which the growth slows and the change in particle diameter can be expressed by a power law, where  $D \propto t^{1/3}$ . The coefficient of variation (Figure S8) drops sharply in the early stages of the reaction from 0.187 to 0.085 indicating size focusing. This further decreases to 0.066 and is maintained at this level for the remainder of the reaction, which indicates a tight size distribution throughout the entire growth regime.

This behavior matches well with our proposed extended LaMer mechanism where we expect to observe a lengthy period of steady state particle growth as particle diameter grows at  $t^{1/3}$  (Figure 3c). Particle volume however shows a linear dependence on time for this steady state growth regime (Figure 3d). By looking closely at the data from the first four aliquots taken (Figure 3d, inset), however, we see a different regime early in the reaction, with a growth rate nearly an order of magnitude larger. This region of the graph corresponds to stage III of the extended LaMer mechanism, where rapid growth occurs during the partial relief of supersaturation. It is interesting to note that

this region also appears to be approximately linear, though with much larger deviations in the linear fit (Figure S8). This increased error is likely a result of the speed of growth in this region, which makes the few seconds of timing error inherent in the manual aliquot withdrawal more apparent in the data. This regime of extremely rapid growth can be attributed to catalytic decomposition of precursor at the surface of the growing particles and is discussed in the following.

**Reproducibility and Predictability.** Reproducibility in nanoparticle synthesis is a significant challenge because nanoparticles are a kinetically determined product, and the kinetics of these reactions can be extremely complex.<sup>1,26</sup> The extended LaMer mechanism, however, allows for improved reproducibility thanks to the simplified kinetics of the steady state growth stage. This is demonstrated in three identical reactions (Figure 4a). To ensure reproducibility is robust for the entire process, different batches of iron oleate precursor were synthesized for each of these reactions. Growth of nanoparticles is very similar for all three reactions, with diameter growing as  $t^{1/3}$  for all reactions (linear plots of nanoparticle volume given in Figure S9). The coefficient of variation in the size of the growing particles between the various reactions remains below 0.04 for all values plotted, which is comparable to the observed size dispersity of a single

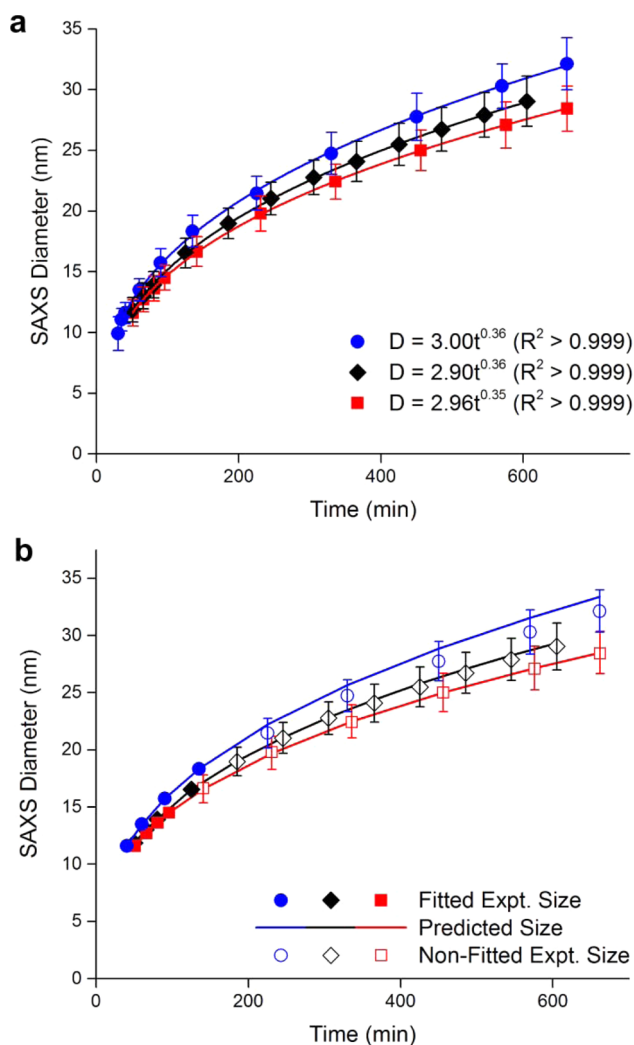


**Figure 4.** Reproducibility and predictability experiments for the extended LaMer synthesis of magnetite nanoparticles. Each line represents a different batch of iron(III) oleate precursor. (a) SAXS diameter against time. Coefficient of variation between reactions is  $<0.04$ . (b) Predictability experiments. Each line corresponds to a reaction carried out with a different batch of iron(III) oleate precursor (see panel a). By measuring the nanoparticle diameter of four aliquots taken after a steady state growth regime is reached (solid symbols), the growth rate can be defined and projected nanoparticle sizes calculated (solid lines). Experimental data show that, at every time point, the predicted nanoparticle size and the observed nanoparticle size (hollow symbols) agree to within 1.5% and have a coefficient of variation of  $<0.01$ .

reaction. The curves fit the data in the steady state growth regime so well that we can use them to predict final nanoparticle size (Figure 4b). To achieve this, aliquots are taken at regular intervals after nucleation is observed, and the average nanoparticle diameter is measured using SAXS (though a variety of other sizing methods could be used). Once a steady state growth regime has been established, four further aliquots are measured. We can then fit these four points to calculate the steady state growth rate and extrapolate to future times to determine when the reaction will yield a desired nanoparticle size. In the examples here, we are extrapolating more than 400 min into the future to reach the final time points, yet at every time point, the size is predicted to within 1.5% of the measured value. For systems where extremely precise size control is

necessary, a reaction could be started, four aliquots collected after steady-state growth has stabilized (here, this is about 20 min after nucleation), and their sizes measured. The growth trajectory could then be plotted and extrapolated, allowing for identification of the time when the desired nanoparticle size will be grown, to a high degree of confidence. The growth trajectory can also be easily altered to yield faster or slower growth by varying reaction parameters such as drip rate or surfactant concentration (Figure S10a). By removing oleic acid from the reaction solution, the particle growth rate can be increased significantly, with nanoparticles up to 62 nm formed in under 90 min (Figure S10b,c).

While batch-to-batch reproducibility observed in Figure 4, panel a is extremely good, there is still the question of what phenomenon causes the batch-to-batch variation in particle sizes. Since the reactions all have precursor added at identical rates, during steady-state growth, they must produce material at the same rate, so the divergence in mean particle size is caused by differing numbers of growing nanoparticles. This is why additional precision in size control is achieved by determining the steady-state growth of an individual reaction. This method controls for the variation in the number of nuclei formed and accounts for the change in growth rate that this causes. By accounting for the number of growing nanoparticles in this manner, we can improve on the 4% coefficient of variation in batch-to-batch particle size to control size to within less than 1%.

**Mechanisms of Growth.** We then can apply the proposed extended LaMer mechanism to our experimental data. Since reagent is added in a controlled, continuous fashion, and nanoparticle size repeatedly measured, we can calculate the quantity of unreacted iron at any given time point in the reaction. The amount of unreacted iron is directly related to monomer concentration in solution by an unknown rate constant. We then plot the concentration of unreacted iron as a function of time, knowing that this is a qualitative representation of a LaMer style plot of monomer concentration (Figure 5). This plot can be divided into four stages, which agree closely with the proposed extended LaMer mechanism in Figure 1, panel b.

However, there is one area of poor agreement in stage III, immediately following nucleation. Here, there is an extremely rapid drop in unreacted iron concentration that is temporally aligned with the size focusing observed in Figure S8. This can be attributed to rapid catalytic growth of the nanoparticles as has previously been described by the Finke-Watzky mechanism.<sup>27,28</sup> This mechanism describes a catalytic reaction at the surface of the growing particle as the rate limiting step and does not involve diffusion of a reactive intermediate to the surface. For a period, this mechanism appears to be the dominant growth mechanism, though it eventually yields to behavior that is consistent with LaMer's mechanism after the nanoparticles are sufficiently large to lose their high catalytic activity (for full discussion, see Supporting Information). While this is the first report of a fast catalytic step in the growth of iron oxide nanoparticles through the thermolysis of iron oleate, it is consistent with observations in the literature that imply that a rapid, exothermic reaction occurs just after nucleation in this system.<sup>14</sup>

This region of catalytic growth is important to note and understand, but it does not dramatically affect the mechanism of size control as the majority of the reaction occurs in a steady-state fashion as described for the extended LaMer mechanism.

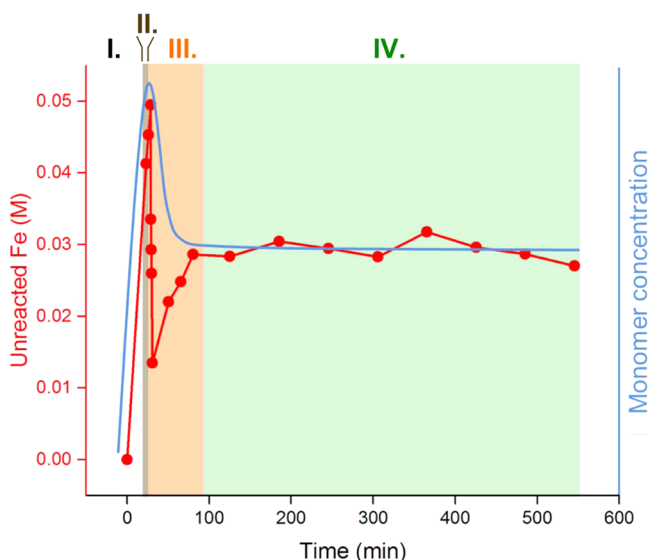


**Figure 5.** Experimental data of the unreacted iron precursor (red) are overlaid by a schematic representing the extended LaMer approach to nanoparticle synthesis (blue). The deviation of the experimental data below 100 min can be attributed to rapid catalytic growth. The four stages of the extended LaMer mechanism are shaded to identify their approximate boundaries.

**Systematic Control of Magnetic Properties.** Ultimately, the goal of size control of nanoparticles is to control their size-dependent properties, and therefore any discussion of size control without addressing the property variations would be incomplete. Here, we measured the magnetic properties of a number of different sized nanoparticles and then investigated the effect that size had on specific absorption rate (SAR), the magnetic hyperthermia figure of merit.

Figure 6 shows the systematic variation of superparamagnetic blocking temperatures ( $T_b$ ) for a series of nanoparticle sizes synthesized by the extended LaMer mechanism. Blocking temperature is a critical property for magnetic nanoparticle applications as it determines whether particles are ferromagnetic or superparamagnetic at a given temperature.<sup>29</sup> As expected,  $T_b$  varies linearly with particle volume (Figure S11).<sup>30</sup> It is worth noting that magnetic nanoparticles have a maximum susceptibility at their blocking temperature.<sup>1,30</sup> This is important for almost all applications, as any given set of particles will produce their maximum magnetic response for a field applied at their blocking temperature. As observed here, the exquisite size control afforded by the extended LaMer mechanism allows for the synthesis of magnetic nanoparticles with a blocking temperature tuned for the target application. Further analysis on the dependence of magnetic susceptibility on nanoparticle size is given in Figure S12.

While blocking temperature and susceptibility are both size dependent, superparamagnetic relaxation time is dramatically more so due to its  $e^{-3}$  dependence. Figure 6, panel b depicts the dependence of the SAR in magnetic hyperthermia on particle size for the iron oxide nanoparticles prepared by the extended LaMer mechanism. Coplotted in this graph is the theoretical shape of the SAR dependence upon size.<sup>31</sup> The dependence upon size is so large that changing average particle size by as little as 2 nm can lead to an order of magnitude change in the rate of heat delivery. MPI and magnetic relaxometry have similarly stringent size requirements, where altering particle size

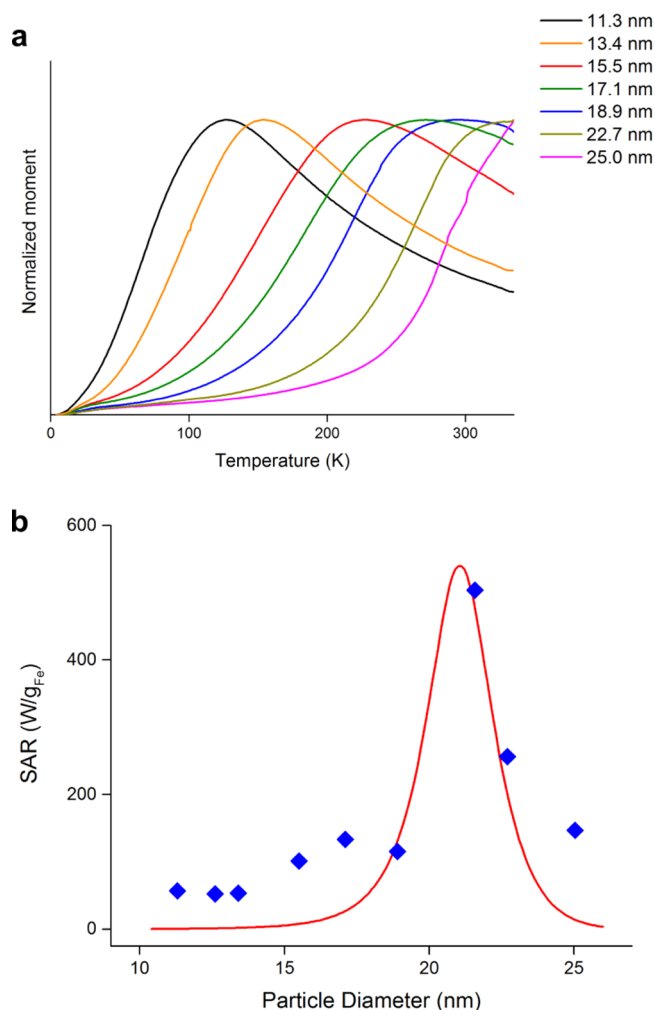


**Figure 6.** (a) Normalized plot of variation in the blocking temperature ( $T_b$ ) with nanoparticle size. (b) Plot of SAR versus nanoparticle diameter for nanoparticles synthesized in the extended LaMer mechanism (blue). Overlaid is the theoretical shape for the SAR dependence on particle size (red).

by 1 nm can render nearly ideal particles difficult to detect.<sup>32</sup> The ability to carefully tune size using the extended LaMer mechanism allows us not only to optimize particles for this application, but also to experimentally confirm the theoretical size dependence of the nanoparticle response.

**Conclusions and Outlook.** We have demonstrated an approach to the synthesis of magnetite nanoparticles that is based on the continuous addition of iron oleate precursor to a heated flask, and we have understood the results using what we term the extended LaMer mechanism. While we have focused on a single system, the extended LaMer approach to nanoparticle synthesis should be broadly applicable to the size-controlled synthesis of a wide range of nanoparticles. We have also demonstrated the ability to predict the size achieved at later points in the reaction by monitoring the size developed early in the reaction. While we have performed this monitoring using SAXS, other systems would be amenable to other size-determination techniques such as light scattering, UV–visible spectroscopy for particles with plasmon resonances, or fluorescence spectroscopy for quantum dots. Because of the steady-state reaction conditions, predictability of the growth rate is a general feature of this growth mechanism and can be



exploited in any system where it is deployed. We expect that this reaction method will be scalable to commercial quantities and are planning experiments to demonstrate this.

## ■ EXPERIMENTAL SECTION

**Synthesis of Iron Oleate Intermediate.** For the synthesis of iron(III) oleate precursor, a 100 mL three-necked round-bottom flask was charged with 3.3 g (9.3 mmol) of  $\text{Fe}(\text{acac})_3$  and 15 mL (47.3 mmol) of oleic acid. The reaction flask was equipped with a thermocouple for monitoring of the reaction temperature. Reactions were performed with vigorous stirring provided by a compact overhead stirrer under a nitrogen atmosphere. The reaction was heated in a 320 °C in a molten metal bath containing Bolton 174, a low melting point metal alloy. The formation of the iron(II) oleate intermediate was first observed at 290 °C. Thirty minutes after 290 °C was exceeded, the reaction was quenched by being removed from the heating bath, and the precursor, with a precisely known iron concentration, was used without any further purification.

**Synthesis of Magnetite Nanoparticles Using the Extended LaMer Mechanism.** For the synthesis of magnetite nanoparticles, a reaction flask containing 2.5 g of docosane and 2.5 mL of oleic acid was heated to 350 °C in a molten metal bath with rapid stirring under a nitrogen atmosphere. To facilitate injection, the as-synthesized iron(III) oleate precursor was diluted in 1-octadecene to give a total iron concentration of 0.22 M. The diluted iron(III) oleate solution was then loaded into a syringe, to which a 6 inch penetration needle was attached. The solution was then dripped into the reaction flask after its temperature had stabilized at 350 °C, at a rate of 3 mL/h using a syringe pump. The start of the reaction,  $t_0$ , was noted as the first drop of precursor was introduced into the reaction solution. Nanoparticle nucleation was observed by an instantaneous change in the color of the reaction solution from dark brown to black. Aliquots were withdrawn from the reaction as close as possible to the nucleation event and at periodic intervals thereafter.

**Characterization. Fourier Transform Infrared (FTIR) Analysis.** Infrared spectra of the iron oleate intermediate were collected on a Bruker IFS 66vS infrared spectrometer (Bruker Optik GmbH, Germany). Aliquots were characterized using a grazing angle attenuated total reflectance (GATR) accessory with a fixed 65° incidence angle and a hemispherical germanium crystal (Harrick Scientific Products Inc., Pleasantville, NY). Two-hundred fifty-six scans of each sample were collected at 2  $\text{cm}^{-1}$  resolution from 3400–700  $\text{cm}^{-1}$  using a liquid nitrogen cooled mercury cadmium telluride (MCT) detector. Extended attenuated total reflectance (ATR) correction was performed on the collected spectra using Opus 6.5 software assuming an index of refraction of 1.5 for the aliquots.

**Transmission Electron Microscopy (TEM).** Samples were prepared by applying a drop of a dilute suspension of nanoparticles in hexanes onto a carbon-coated copper grid. Bright field TEM studies were performed using a JEOL 1200EX TEM operating at 120 kV. High-resolution (HR)TEM images were acquired using a Tecnai G2 F30 TEM using a 300 keV acceleration voltage. Size analysis of imaged particles was performed using ImageJ software.

**Small Angle X-ray Scattering (SAXS).** For near real time analysis of the growth of magnetite nanoparticles, withdrawn aliquots were suspended in a small volume of hexanes and injected into glass capillary tubes with a 1.0 mm diameter. Aliquots were then analyzed using a Rigaku SmartLab diffractometer system with the SmartLab Guidance system control software. Cu–K-alpha radiation (40 kV, 44 mA) was used in transmission geometry with a scintillation detector. Data analysis was performed using Rigaku NANO-Solver v. 3.5 software. The model form factor chosen for analysis was a spherical particle shape with a Gaussian size distribution.

**Specific Absorption Rate Measurements.** The rate of energy dissipation of the nanoparticles was evaluated by application of an alternating magnetic field (36.5 kA/m, 341 kHz) generated using an eight-turn coil (1.2 in ID, 3.25 in length) and an induction heater. Liquid samples (200  $\mu\text{L}$ ) were placed in a glass vial in a plastic holder inside a cooling jacket. Sample temperature was monitored using a

fiber-optic temperature probe. The sample was allowed to reach thermal equilibrium prior to turning on the magnetic field. Temperature was recorded at 0.2 s intervals. The SAR of the sample was determined from the product of the initial slope of the temperature versus time curve, the total mass of the sample, and the heat capacity of the sample (assumed to be that of the solvent), divided by the mass of iron determined from a spectrophotometric assay.

## ■ ASSOCIATED CONTENT

### § Supporting Information

The Supporting Information is available free of charge on the ACS Publications website at DOI: 10.1021/acs.chemmater.5b02510.

Full material and experimental details, full discussion and FTIR analysis of iron oleate intermediate formation, HRTEM, XRD, SQUID, addition size analysis, and additional discussion on size dependent magnetic properties (PDF)

## ■ AUTHOR INFORMATION

### Corresponding Author

\*E-mail: Dale.Huber@sandia.gov.

### Notes

The authors declare no competing financial interest.

## ■ ACKNOWLEDGMENTS

This research was supported by the U.S. Department of Energy, Office of Basic Energy Sciences, Division of Materials Science and Engineering. HRTEM imaging and XRD/SAXS measurements were performed at the Center for Integrated Nanotechnologies, a U.S. Department of Energy, Office of Basic Energy Sciences user facility. We acknowledge Hongfei Bao for assistance with magnetic measurements of samples. Sandia National Laboratories is a multiprogram laboratory managed and operated by Sandia Corporation, a wholly owned subsidiary of Lockheed Martin Corporation, for the U.S. Department of Energy's National Nuclear Security Administration under Contract No. DE-AC04-94AL85000.

## ■ REFERENCES

- (1) Huber, D. L. Synthesis, properties, and applications of iron nanoparticles. *Small* **2005**, *1*, 482–501.
- (2) Herman, D. A. J.; Ferguson, P.; Cheong, S.; Hermans, I. F.; Ruck, B. J.; Allan, K. M.; Prabakar, S.; Spencer, J. L.; Lendrum, C. D.; Tilley, R. D. Hot-injection synthesis of iron/iron oxide core/shell nanoparticles for T-2 contrast enhancement in magnetic resonance imaging. *Chem. Commun.* **2011**, *47*, 9221–9223.
- (3) Cheong, S.; Ferguson, P.; Hermans, I. F.; Jameson, G. N. L.; Prabakar, S.; Herman, D. A. J.; Tilley, R. D. Synthesis and Stability of Highly Crystalline and Stable Iron/Iron Oxide Core/Shell Nanoparticles for Biomedical Applications. *ChemPlusChem* **2012**, *77*, 135–140.
- (4) Sun, S.; Zeng, H. Size-controlled synthesis of magnetite nanoparticles. *J. Am. Chem. Soc.* **2002**, *124*, 8204–8205.
- (5) Yin, Y.; Alivisatos, A. P. Colloidal nanocrystal synthesis and the organic-inorganic interface. *Nature* **2005**, *437*, 664–670.
- (6) Murray, C. B.; Kagan, C. R.; Bawendi, M. G. Synthesis and characterization of monodisperse nanocrystals and close-packed nanocrystal assemblies. *Annu. Rev. Mater. Sci.* **2000**, *30*, 545–610.
- (7) Adolphi, N. L.; Huber, D. L.; Jaetao, J. E.; Bryant, H. C.; Lovato, D. M.; Fegan, D. L.; Venturini, E. L.; Monson, T. C.; Tessier, T. E.; Hathaway, H. J.; Bergemann, C.; Larson, R. S.; Flynn, E. R. Characterization of magnetite nanoparticles for SQUID-relaxometry

and magnetic needle biopsy. *J. Magn. Magn. Mater.* **2009**, 321, 1459–1464.

(8) Adolphi, N. L.; Butler, K. S.; Lovato, D. M.; Tessier, T. E.; Trujillo, J. E.; Hathaway, H. J.; Fegan, D. L.; Monson, T. C.; Stevens, T. E.; Huber, D. L.; Ramu, J.; Milne, M. L.; Altobelli, S. A.; Bryant, H. C.; Larson, R. S.; Flynn, E. R. Imaging of Her2-targeted magnetic nanoparticles for breast cancer detection: comparison of SQUID-detected magnetic relaxometry and MRI. *Contrast Media Mol. Imaging* **2012**, 7, 308–319.

(9) Khandhar, A. P.; Ferguson, R. M.; Arami, H.; Krishnan, K. M. Monodisperse magnetite nanoparticle tracers for in vivo magnetic particle imaging. *Biomaterials* **2013**, 34, 3837–3845.

(10) Arami, H.; Krishnan, K. M. Highly Stable Amine Functionalized Iron Oxide Nanoparticles Designed for Magnetic Particle Imaging (MPI). *IEEE Trans. Magn.* **2013**, 49, 3500–3503.

(11) Deatsch, A. E.; Evans, B. A. Heating efficiency in magnetic nanoparticle hyperthermia. *J. Magn. Magn. Mater.* **2014**, 354, 163–172.

(12) Giordano, M. A.; Gutierrez, G.; Rinaldi, C. Fundamental solutions to the bioheat equation and their application to magnetic fluid hyperthermia. *Int. J. Hyperthermia* **2010**, 26, 475–484.

(13) Park, J.; Lee, E.; Hwang, N. M.; Kang, M. S.; Kim, S. C.; Hwang, Y.; Park, J. G.; Noh, H. J.; Kim, J. Y.; Park, J. H.; Hyeon, T. One-nanometer-scale size-controlled synthesis of monodisperse magnetic iron oxide nanoparticles. *Angew. Chem., Int. Ed.* **2005**, 44, 2872–2877.

(14) Park, J.; An, K. J.; Hwang, Y. S.; Park, J. G.; Noh, H. J.; Kim, J. Y.; Park, J. H.; Hwang, N. M.; Hyeon, T. Ultra-large-scale syntheses of monodisperse nanocrystals. *Nat. Mater.* **2004**, 3, 891–895.

(15) Kwon, S. G.; Piao, Y.; Park, J.; Angappane, S.; Jo, Y.; Hwang, N. M.; Park, J. G.; Hyeon, T. Kinetics of monodisperse iron oxide nanocrystal formation by “heating-up” process. *J. Am. Chem. Soc.* **2007**, 129, 12571–12584.

(16) Yu, W. W.; Falkner, J. C.; Yavuz, C. T.; Colvin, V. L. Synthesis of monodisperse iron oxide nanocrystals by thermal decomposition of iron carboxylate salts. *Chem. Commun.* **2004**, 2306–2307.

(17) Kwon, S. G.; Hyeon, T. Formation Mechanisms of Uniform Nanocrystals via Hot-Injection and Heat-Up Methods. *Small* **2011**, 7, 2685–2702.

(18) Bronstein, L. M.; Huang, X.; Retrum, J.; Schmucker, A.; Pink, M.; Stein, B. D.; Dragnea, B. Influence of iron oleate complex structure on iron oxide nanoparticle formation. *Chem. Mater.* **2007**, 19, 3624–3632.

(19) Thanh, N. T. K.; Maclean, N.; Mahiddine, S. Mechanisms of Nucleation and Growth of Nanoparticles in Solution. *Chem. Rev.* **2014**, 114, 7610–7630.

(20) LaMer, V. K.; Dinegar, R. H. Theory, Production and Mechanism of Formation of Monodispersed Hydrosols. *J. Am. Chem. Soc.* **1950**, 72, 4847–4854.

(21) Sugimoto, T. Preparation of Monodispersed Colloidal Particles. *Adv. Colloid Interface Sci.* **1987**, 28, 65–108.

(22) Lifshitz, I. M.; Slyozov, V. V. The kinetics of precipitation from supersaturated solid solutions. *J. Phys. Chem. Solids* **1961**, 19, 35–50.

(23) Wagner, C. Z. Theory of precipitate change by redissolution. *Zeitschrift fuer Elektrochemie und Angewandte Physikalische Chemie* **1961**, 65, 581–591.

(24) Cullity, B. D.; Graham, C. D. Ferrimagnetism. In *Introduction to Magnetic Materials*, 2nd ed.; Wiley-IEEE Press: Picataway, NJ, 2009; pp 175–195.

(25) Koerner, H.; MacCuspie, R. I.; Park, K.; Vaia, R. A. In Situ UV/Vis, SAXS, and TEM Study of Single-Phase Gold Nanoparticle Growth. *Chem. Mater.* **2012**, 24, 981–995.

(26) Watt, J.; Cheong, S.; Tilley, R. D. How to control the shape of metal nanostructures in organic solution phase synthesis for plasmonics and catalysis. *Nano Today* **2013**, 8, 198–215.

(27) Watzky, M. A.; Finke, R. G. Transition Metal Nanocluster Formation Kinetic and Mechanistic Studies. A New Mechanism When Hydrogen Is the Reductant: Slow, Continuous Nucleation and Fast Autocatalytic Surface Growth. *J. Am. Chem. Soc.* **1997**, 119, 10382–10400.

(28) Watzky, M. A.; Finney, E. E.; Finke, R. G. Transition-metal nanocluster size versus formation time and the catalytically effective nucleus number: A mechanism-based treatment. *J. Am. Chem. Soc.* **2008**, 130, 11959–11969.

(29) Cullity, B. D. *Introduction to Magnetic Materials*; Addison-Wesley Publishing Company: Boston, MA, 1972; p 666.

(30) Papaefthymiou, G. C. Nanoparticle magnetism. *Nano Today* **2009**, 4, 438–447.

(31) Rosensweig, R. E. Heating magnetic fluid with alternating magnetic field. *J. Magn. Magn. Mater.* **2002**, 252, 370–374.

(32) Adolphi, N. L.; Huber, D. L.; Bryant, H. C.; Monson, T. C.; Fegan, D. L.; Lim, J.; Trujillo, J. E.; Tessier, T. E.; Lovato, D. M.; Butler, K. S.; Provencio, P. P.; Hathaway, H. J.; Majetich, S. A.; Larson, R. S.; Flynn, E. R. Characterization of single-core magnetite nanoparticles for magnetic imaging by SQUID relaxometry. *Phys. Med. Biol.* **2010**, 55, S985–6003.